RSC Advances

PAPER

View Article Online
View Journal | View Issue

Cite this: *RSC Adv.*, 2024, **14**, 32759

6-Aminocoumarin-derived Schiff base gelators: aggregation and sensing of CN^-, Fe^{3+}, Cu^{2+} and CO_2 under different conditions†

Eshani Paul, Rameez Raza, Subrata Ranjan Dhara, Nabajyoti Baildya and Kumaresh Ghosh *

Herein, we report the synthesis, characterization, supramolecular gelation and multiple applications of 6-aminocoumarin-derived Schiff bases **1** and **2**. Both Schiff bases underwent gelation in DMF–H_2O (2 : 1, v/v), DMSO–H_2O (2 : 1, v/v) and dioxane–H_2O (2 : 1, v/v) involving weak forces. Furthermore, the gels were stable and exhibited good viscoelastic properties. The storage modulus (G') of each gel was considerably higher than its loss modulus (G''). The higher value of the crossover point and lower value of tan δ for the gel of Schiff base **2** compared to the gel of Schiff base **1** demonstrated the better gelation behaviour of **2** than that of **1** in DMF–H_2O (2 : 1, v/v). Further, iodo-analogue **2** exhibited cross-linked helical morphology, whereas non-iodo analogue **1** exhibited long chain fibrous morphology, as observed *via* FESEM. These differences in morphology and viscoelastic behaviors were attributed to the iodo group present in **2**, which influenced its aggregation involving halogen bonding. To demonstrate their application, the DMF–H_2O (2 : 1, v/v) gels of both **1** and **2** recognized CN^- over a series of other anions by exhibiting a gel-to-sol phase change. Besides anion sensing, gels **1** and **2** selectively detected Fe^{3+} and Cu^{2+} ions over other metal ions *via* a gel-to-gel colour change. Finally, CN^--treated solutions of **1** and **2** allowed the successful detection of CO_2 by the naked eye. Moreover, the detection was possible using a test-kit method.

Received 29th July 2024
Accepted 20th September 2024

DOI: 10.1039/d4ra05503a

rsc.li/rsc-advances

Introduction

The design and synthesis of multiple application-based low molecular weight Schiff base gelators and their structural tuning by introducing new functional groups are of contemporary interest in supramolecular chemistry.[1] Owing to the dynamic reversibility of imine bonds and their potential for metal coordination, Schiff base gelators represent a particular type of unique and versatile gel-forming assembly building blocks.[2] This allows the corresponding gel to be highly responsive to various external triggers, such as pH,[3] metal cations,[4] and anions.[5] Consequently, supramolecular gels constructed from Schiff base compounds show tremendous promise for ion detection,[6] catalysis,[7] optical emissions,[8] *etc*.

Similar to other supramolecular gelators, Schiff base gelators show aggregation *via* weak interactions such as hydrogen bonding, electrostatic interactions, hydrophobic, and π–π stacking interactions or their combination.[9]

Among the different types of non-covalent interactions, halogen bonding[10] as an equivalent to hydrogen bonding[11] often plays a major or minor role during aggregation depending on the position of the halogen group in the structure. Thus, halogen bonding-induced supramolecular assembly has recently gained interest because of its unique features and prospective.[12]

However, despite the remarkable work on Schiff base gelators of different architectures,[13] the use of a coumarin motif in this capacity is less explored. Importantly, coumarin for its optical properties has been widely used for recognition of ions in solution.[14] Alternatively, exploitation of this motif in gel-phase sensing of ions is scarce. Especially, the 6-aminocoumarin-based Schiff base and its possible applications are unknown in supramolecular gelation. In a report by M. K. Paul *et al.*, they investigated the liquid crystal properties of some 6-aminocoumarin-derived Schiff bases and examined their zinc-complexing behavior. In addition, they noted their gelation properties on modifying the alkoxy chains of the compounds.[15]

In continuation of our work on the recognition and sensing of ions in solution and gel states, herein we report the synthesis of 6-aminocoumarin-based Schiff bases **1** and **2** (Fig. 1), which

Department of Chemistry, University of Kalyani, Kalyani 741235, India. E-mail: ghosh_k2003@yahoo.co.in; kumareshchem18@klyuniv.ac.in; Fax: +91 3325828282; Tel: +91 3325828750-305

† Electronic supplementary information (ESI) available: Gelation results, gel pictures, spectral comparison, Hirshfeld analysis, Benesi–Hildebrand and detection limit, binding constant curves, Jobs plots, Stern–Volmer plots, Crystallographic data, copies of ^1H, ^{13}C and HRMS spectra. CCDC 2361386. For ESI and crystallographic data in CIF or other electronic format see DOI: https://doi.org/10.1039/d4ra05503a

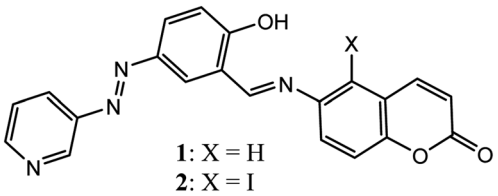

Fig. 1 Structures of compounds 1 and 2.

undergo gelation in DMF–H_2O (2 : 1, v/v), DMSO–H_2O (2 : 1, v/v) and dioxane–H_2O (2 : 1, v/v). Compound **2** was considered in this study to understand the role of halogen bonding in its aggregation. The rheological experiments showed that the viscoelastic characteristics of the gels of **1** and **2** differed significantly. During aggregation, compounds **1** and **2** followed different patterns of molecular packing, as reflected in their FESEM images. These different properties were attributed to the role of iodine in the weak halogen bonding. The gels in DMF : H_2O (2 : 1, v/v) were stimuli responsive and selective for CN^- ions among other anions studied. Besides anion sensing, gels **1** and **2** exhibited selective responses to Fe^{3+} and Cu^{2+} ions among other metal ions, resulting in a gel-to-gel colour change. As an extension of their application, CN^--treated DMF–H_2O (2 : 1, v/v) solutions of **1** and **2** detected CO_2 through a colour change. The test-kit detection boosts this investigation. Furthermore, the optical properties of the Schiff bases changed with the pH of the medium.

CN^- recognition has attracted attention because of its importance in biology and the environment. It is exceedingly poisonous and detrimental to both human health and the environment.[16] Thus, for the gel-phase recognition of this ion, the different interactional properties of CN^- include nucleophilic attack on a reactive functional group in a molecule or on a metal centre in a metal–ligand complex, as well as participation in H-bonding, followed by deprotonation.[17]

Besides CN^- sensing, the detection of physiologically and environmentally relevant transition metal ions is a major concern in analytical chemistry.[18] Among the different transition metal ions, Cu^{2+} and Fe^{3+} are two necessary trace metal ions found in the human body. Their balance in the body is essential.[19] A shortage of iron in the body leads to anaemia, liver damage, Alzheimer's and Parkinson's disease, *etc.*[20] Similarly, excessive levels of Cu^{2+} produce oxidative stress and problems linked to neuro degenerative illnesses such as Alzheimer's, Wilson's, and Menke's disease.[21] Thus, a simple and effective method for the detection of Fe^{3+} and Cu^{2+} ions, particularly in a sol–gel medium, has attracted attention.

Besides ion sensing, the recognition of CO_2 as a neutral molecule has attracted attention given that it plays an important role in human physiology. Also, it has impact on agriculture, food, and chemical industries.[22] The selective and quick colorimetric detection of this neutral gaseous molecule by employing an anion-responsive synthetic compound, which has been infrequently reported in the literature, is commendable in recognition chemistry.[23]

Results and discussion

Synthesis

Compounds **1** and **2** were synthesised according to Scheme 1. 6-Aminocoumarin **3** and 7-iodo-6-aminocoumarin **4**, which were prepared from coumarin according to the reported procedures, were reacted with pyridyl-azo salicylaldehyde **5** in dry MeOH at room temperature to give compounds **1** and **2** in reasonable yields, respectively. Both **1** and **2** were characterized by ^1H, ^{13}C NMR and mass spectral analyses.

Gelation and gel characterization

Although coumarin was employed in the designs due to its excellent optical characteristics, a 3-pyridylazo salicylaldehyde unit was used to aid solvent gelation. Thus, to test the gelation abilities of compounds **1** and **2**, various solvents with different polarities were selected. Table S1† summarizes the details of the gel study including the minimum gelation concentration (MGC) and T_g (gel-to-sol transition temperature) values. Both **1** and **2** were gelled in the same solvent combination. Gel formation was not observed in benzenoid or semi-aqueous solvents. However, they were stable and thermo-reversible (Fig. S1†). The gels exhibited different T_g and MGC values (Table S1†). Compound **1** produced a gel at a somewhat lower MGC compared to compound **2** (Table S1†). This emphasized the better gelation propensity of **1** over **2**, which was attributed to the size factor or some dipole–dipole interaction of the iodo group in structure **2**.

However, the effect of the iodo group in gelator **2** with respect to gelator **1** was comprehensible from the viscoelastic properties of the gels prepared in DMF–H_2O (2 : 1, v/v). In the frequency sweep experiment, the storage modulus (G') of the gels was observed to be higher than the loss modulus (G''), reflecting the true nature of the gels (Fig. 2). Further, the amplitude sweep experiments of the gels in DMF–H_2O (2 : 1, v/v) were performed at a constant frequency of 1 Hz. To compare the viscoelastic properties of the gels of **1** and **2**, rheological data were acquired using freshly prepared gels at their minimum gelation concentrations and identical concentrations (6 mg mL^{-1}) (Fig. 2 and Table 1). The analysis revealed that the critical strain of the DMF–H_2O (2 : 1, v/v) gel of **2** was greater than that of the gel of **1**. This corroborates that the gel of **2** had higher mechanical strength than that of the gel of **1**.

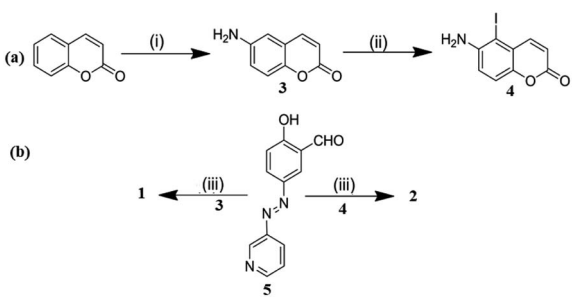

Scheme 1 (i) (a) HNO_3 : H_2SO_4 (1 : 3, v/v), stirring, rt, 1 h, (b) Fe-powder, NH_4Cl, H_2O, reflux, 2–3 h; (ii) NIS (*N*-iodosuccinimide), dry CH_2Cl_2, rt, stirring, 12 h; and (iii) MeOH, rt, stirring, 2 h.

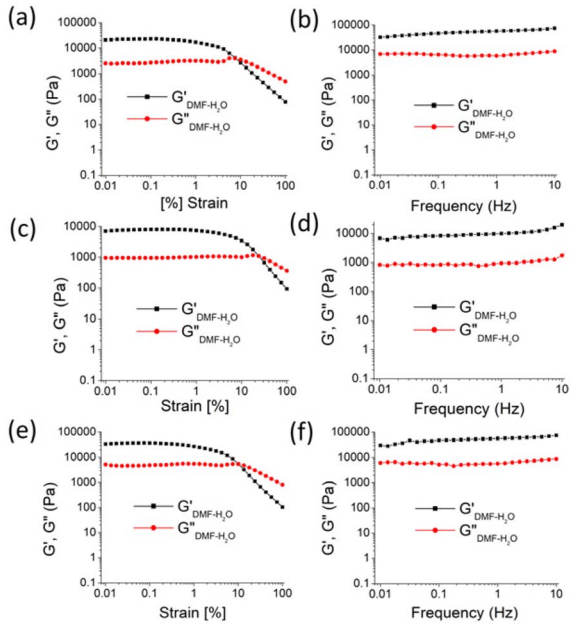

Fig. 2 Rheology study of the gels of **1** and **2**: (a and c) amplitude sweep (at a constant frequency of 1 Hz) and (b and d) frequency sweep (at a constant 0.01% strain) experiments. Gels were prepared in DMF–H_2O (2 : 1, v/v) at the MGC [MGC = 5 mg mL^{-1}, *i.e.*, $c = 1.35 \times 10^{-2}$ M for gel of **1** and MGC = 6 mg mL^{-1}, *i.e.*, $c = 1.20 \times 10^{-2}$ M for gel of **2**], and the experiments were carried out at 25 °C. Rheology study of the gel of **1** at the MGC of **2** [MGC = 6 mg mL^{-1}, $c = 1.62 \times 10^{-2}$ M]: (e) amplitude sweep (at a constant frequency of 1 Hz) and (f) frequency sweep (at constant 0.01% strain) experiments.

Similar observations were found at the crossover point. The crossover point of the DMF–H_2O (2 : 1, v/v) gel of **2** was 3 times higher than that of the gel of **1** in the same solvent. This result indicates that the gel of **2** bears a greater resistance to any change in momentum of a gel medium (Fig. 2 and Table 1). However, in the study, an increase in the gelation concentration increased the crossover point. In this context, the crossover point for the gel of **1** in DMF–H_2O (2 : 1, v/v) was enhanced when the gelation concentration of **1** changed from 5 mg mL^{-1} to 6 mg mL^{-1} (Fig. 2 and Table 1). At the same concentration of gels, the crossover point in the amplitude sweep study for the gel of **2** was still significantly higher than that of the gel of **1**. Further, the lower tan δ of gel of **2** over the gel of **1** demonstrated the better gelation behaviour of **2** in DMF–H_2O (2 : 1, v/v) (Fig. 2 and Table 1). It was further noted that the crossover point and gel strength could be modulated on mixing the gels of **1** and **2**. In this event, the gel obtained from the mixing of gelators **1** and **2** in DMF–H_2O (2 : 1, v/v) resulted in a crossover point lying between the crossover points of the pristine gels of **1** and **2** (Fig. S2 and Table S2†).

However, the dissimilarity in rheological behaviour between the gels **1** and **2** is attributed to the different packing patterns of the gelators during their aggregation. The iodo group in the backbone of **2** may exhibit halogen bonding during aggregation. To gain further insight into the mode of aggregation and iodo effect, we tried to get the crystal structures of **1** and **2**, but we failed. However, the FESEM images of the gels revealed their different morphologies. Although the aggregation of molecules of **1** led to a long chain fibrous morphology, iodo-analogue **2** possessed a cross-linked helical morphology. This is believed to be due to the halogen-bonding role in gelator **2**, which influenced its aggregation pattern. The gel prepared from mixing **1** and **2** possessed a highly cross-linked network morphology (Fig. 3e and f). In describing the fibrous morphology of the gels, role of H-bonding and π-stacking interactions during their aggregation cannot be ignored and it is believed that these weak forces introduced stiffness in the gels.

The comparison of the absorption and fluorescence spectra of **1** and **2** in the solution and gel states also supported their aggregation (Fig. 4). In solution, the strong absorption at 380 nm for **1** in DMF–H_2O (2 : 1, v/v) was blue-shifted to 335 nm

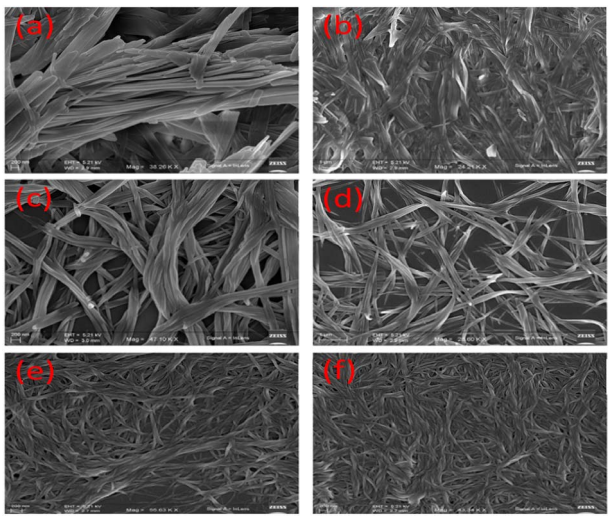

Fig. 3 FESEM images of the gels of **1** (a and b), **2** (c and d) and mixture of **1** and **2** (e and f) in DMF–H_2O (2 : 1, v/v) [$c = 1.35 \times 10^{-2}$ M (for gel of **1**) and $c = 1.20 \times 10^{-2}$ M (for gel of **2**)].

Table 1 Summary of the rheological properties of the gels of **1** and **2** prepared in DMF–H_2O (2 : 1, v/v)[a]

Compound	Critical strain (%)	Crossover (% strain)	G'_{av} (Pa)*	G''_{av} (Pa)*	tan δ (G''_{av}/G'_{av})
1 (5 mg mL^{-1})	0.42	7.83	51 556	8030	0.155
2 (6 mg mL^{-1})	2.37	22.25	12 656	1559	0.12
1 (6 mg mL^{-1})	0.76	10.11	58 164	8143	0.14

[a] G'_{av} and G''_{av} values were calculated from frequency sweep data.

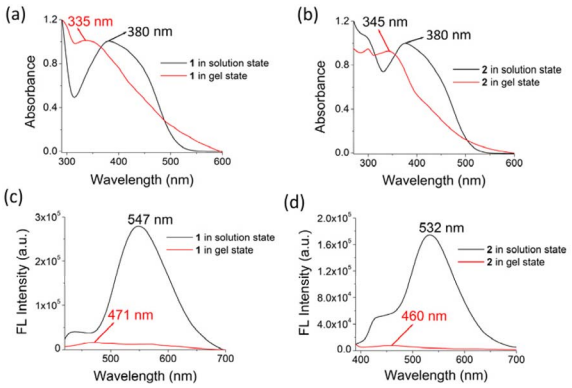

Fig. 4 Comparison of (a and b) normalized UV-vis and (c and d) fluorescence spectra ($\lambda = 380$ nm) of **1** and **2** in the solution ($c = 2.5 \times 10^{-5}$ M) and DMF : H_2O (2 : 1, v/v) gel states [$c = 1.35 \times 10^{-2}$ M (for gel of **1**) and $c = 1.20 \times 10^{-2}$ M (for gel of **2**)].

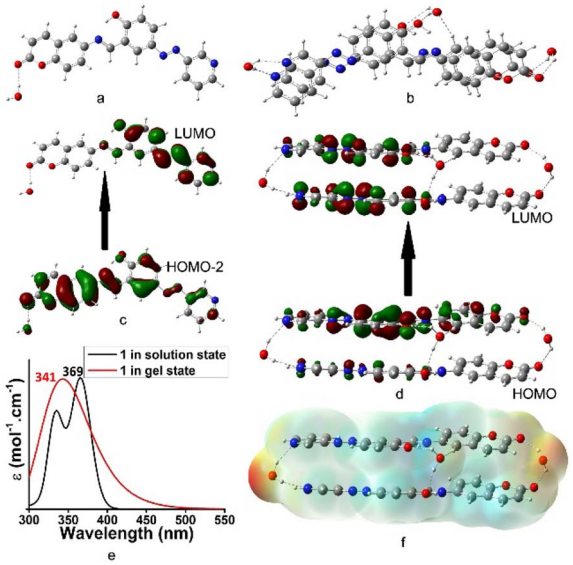

Fig. 5 Optimized geometries of (a) **1**, (b) **1**-aggregation, (c) electronic transition of **1**, (d) electronic transition of aggregated form of **1**, (e) UV-vis of (a) and (b), and (f) electrostatic potential surface of aggregated form of **1**.

in the gel state, whereas the absorption peak at 380 nm in compound **2** in solution was shifted to 345 nm in the gel state. This blue-shift in the absorption bands indicated H-type aggregation.[24] In the fluorescence spectrum, the emission of **1** at 547 nm in DMF–H_2O (2 : 1, v/v) solution moved to 471 nm with a significant reduction in its intensity in the gel state. Similarly, the emission of **2** at 532 nm in DMF–H_2O (2 : 1, v/v) shifted to 460 nm in the gel state with a decrease in intensity (Fig. 4). The quenching of emission in both gels corroborated the aggregation-caused quenching event.[25]

To understand the role of the functional groups in aggregation, we recorded the FT-IR spectra of the gels but failed to reach a conclusion (Fig. S3 and S4†). In the case of **1**, the stretching signals at 1714 cm^{-1} (lactone carbonyl) and 1623 cm^{-1} (imine) were difficult to analyze due to the interference from the amide signal of DMF, which was inherently present in the gel (Fig. S3†). This was also the case for the gel of **2** (Fig. S4†). The amide carbonyl of DMF, appearing as broad signal at 1668 cm^{-1}, obscured the stretching of the lactone and imine functionalities of the compounds (Fig. S3 and S4†).

A theoretical study was performed to realize the mode of aggregation and influence of iodine in this event. The aggregation of **1** at the atomistic level was calculated by DFT simulations.[26] Fig. 5a and b present the optimized geometries of **1** and its aggregation, respectively. In the process of aggregation, the water molecule plays an important role. Fig. 5c and d present the electronic transitions of **1** in the solution and aggregated states, respectively. Although the electronic transition H-2 → L with λ_{max} at 369 nm (expt. 380 nm) was observed in solution, a blue shifted λ_{max} at 341 nm (expt. 335 nm) for the H → L transition was detected in the aggregated state. In this regard, Fig. 5e represents the UV-vis spectra of **1** in solution and in the aggregated states. Fig. 5f represents the electrostatic potential surface (EPS) of the aggregated form of **1**. The active site is shown by red colour.

The aggregation pattern of iodo-analogue **2** was very similar to that of **1**. Fig. 6a and b represent the optimized geometries of **2** and its aggregated form, respectively. Similar to **1**, here water molecules also control the aggregation. The hydrogen-bonded water in the aggregate is further involved in halogen bonding with iodine. This highlighted the different aggregation pattern of **2** from **1**. Fig. 6c and d present the electronic transitions of **2** in the solution and aggregated states, respectively. In solution, the H → L electronic transition corresponds to λ_{max} at 374 nm (exp. 380 nm). In the aggregated state, it was blue-shifted to 343 nm (exp. 345 nm). Fig. 6e presents the theoretical UV-vis spectra of **2** in the solution and aggregated states. Fig. 6f presents the electrostatic potential surface (EPS) of the aggregated

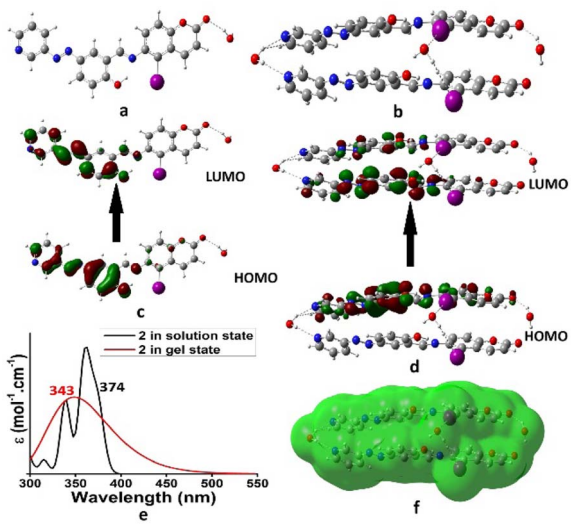

Fig. 6 Optimized geometries of (a) **2**, (b) **2**-aggregation, (c) electronic transition of **2**, (d) electronic transition of aggregated form of **2**, (e) UV-vis of (a) and (b), and (f) electrostatic potential surface of aggregated form of **2**.

form of **2**. The active site differs from **1** and indicates the different aggregation pattern of **2**. Thus, the presence of iodine in **2** has a definite role in the packing of the molecules during their aggregation, resulting in differences in the rheology and morphology between the gels of **2** and **1**.

Effect of pH on gels and solutions

The effect of pH on the solution and gel states of compounds **1** and **2** was studied. The solutions and gels were prepared in DMF–H_2O (2 : 1, v/v; prepared using HEPES buffer, 10 mM) at different pH values (Fig. S5 and S6,† respectively). Importantly, stable gels were obtained in a wide range of pH 2.6 to pH 8. Above pH 8, the gels were gradually disrupted and became a clear solution at pH 13.8 for **2** although under this condition there was some sticky mass in **1**. This dissimilar behaviour was assumed to be due to the different acidic characters of the compounds.

In solution, both **1** and **2** showed different behaviours with a change in pH. Compound **2** displayed color above pH 5, whereas compound **1** produced a light brown color at pH 5. This was due to the ionization of phenol to phenoxide at different pH. At basic pH, solutions of **1** and **2** became orange red due to the charge transfer from the phenoxide ion to the pyridine ring. UV-vis spectra were recorded for the solutions of **1** and **2** at different pH values. Although both compounds showed absorption below 350 nm at acidic pH, their absorption appeared above 350 nm at neutral and basic pH (Fig. S7†). Using the absorption data, the p*K*a values of **1** and **2** were determined to be 5.88 and 6.10, respectively (Fig. S8†).[27] The pH study revealed that both compounds can be used for sensing in a wide pH range.

CN^- recognition

Owing to the presence of phenolic –OH and imine groups in the compounds, we intended to investigate their anion-responsive behavior. It was thought that compounds **1** and **2** should interact with anions either through H-bonding or deprotonation, followed by H-bonding. The interaction may also occur through a nucleophilic addition to the imine bond. There was also interest in learning if there was anion binding dissimilarity for **2** due to the iodo group in its structure, which caused the microstructure and viscoelastic characteristics of its gel to differ from that of **1**. Thus, the DMF–H_2O (2 : 1, v/v) gels of **1** and **2** were carefully explored for anion recognition.

To test the anion-responsive behavior of the gels, either the gels were treated with anions or the formation of the gels was observed in the presence of anions. The gels of **1** and **2** showed different results in the presence of tetrabutylammonium salts of anions such as CN^-, F^-, AcO^-, $H_2PO_4^-$, Cl^-, Br^-, I^-, NO_3^- and HSO_4^- (Fig. 7). Breaking of the gels to a sol only occurred in the presence of CN^- ions presumably due to either deprotonation of the phenolic –OH or nucleophilic attack of CN^- to imine bond in the structures. Other anions (F^-, AcO^-, $H_2PO_4^-$, Cl^-, Br^-, I^-, NO_3^- and HSO_4^-) were unable to cause a either color or phase change in the gels. In this case, CN^- behaved differently from F^- due to the presence of water in the gelling solvent,

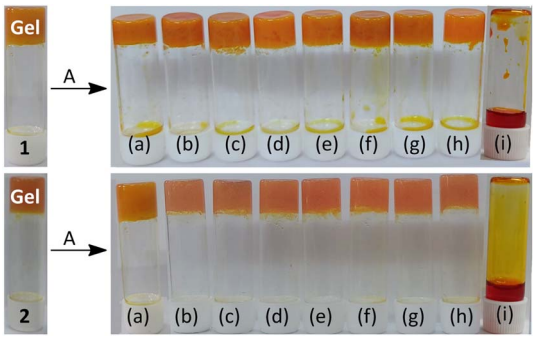

Fig. 7 Change in the DMF–H_2O (2 : 1, v/v) gels of **1** and **2** [$c = 1.35 \times 10^{-2}$ M (for gel of **1**) and $c = 1.20 \times 10^{-2}$ M (for gel of **2**)] upon the addition of 1 equiv. amount of different anions (as tetrabutylammonium salt) after 10 min [from left to right] (a) NO_3^-, (b) F^-, (c) AcO^-, (d) $H_2PO_4^-$, (e) Cl^-, (f) Br^-, (g) I^-, (h) HSO_4^- and (i) CN^-.

which hydrated F^- more strongly than CN^-. Thus, both gels were sensitive and selective to CN^- among the different tested anions. To evaluate the sensitivity of the gels to CN^-, it was found that the gels started to disintegrate upon the addition of 0.5 equiv. of CN^- and became a clear solution in the presence of 1 equiv. of CN^-.

However, to check the anion binding in solution, UV-vis and fluorescence titrations of **1** and **2** [$c = 2.50 \times 10^{-5}$ M] were performed in DMF–H_2O (2 : 1, v/v) with the above-mentioned anions ($c = 1.0 \times 10^{-3}$ M) (Fig. 8). In DMF–H_2O (2 : 1, v/v), anions such as CN^-, F^- and HSO_4^- resulted in noticeable changes in the UV-vis spectra. Other anions such as AcO^-, Cl^-,

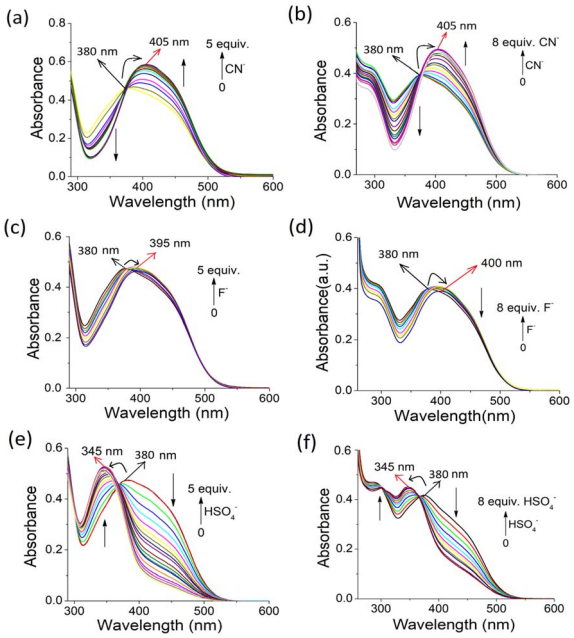

Fig. 8 Change in UV-vis spectra of **1** [$c = 2.50 \times 10^{-5}$ M] upon the addition of (a) CN^-, (c) F^- and (e) HSO_4^- [$c = 1.0 \times 10^{-3}$ M] up to their 5 equiv. amounts in DMF–H_2O (2 : 1, v/v). Change in UV-vis spectra of **2** [$c = 2.50 \times 10^{-5}$ M] upon the addition of (b) CN^-, (d) F^- and (f) HSO_4^- [$c = 1.0 \times 10^{-3}$ M] up to their 8 equiv. amounts in DMF–H_2O (2 : 1, v/v).

Br^-, I^-, $H_2PO_4^-$ and NO_3^- were non-interacting under identical conditions. In the spectrum of **1**, the absorption band at 380 nm in DMF–H_2O (2 : 1, v/v) shifted to 405 nm with a gradual increase in intensity during titration with CN^- ions, resulting in an isosbestic point at 380 nm (Fig. 8a). The spectral change was constant until the addition of 5 equiv. of CN^- ions. A similar change was observed for **2** with CN^- ions, where the increase in absorption intensity at 405 nm became saturated on the addition of 8 equiv. of CN^- ions (Fig. 8b). The CN^--induced red shift in the absorption peak was due to the deprotonation of the phenolic –OH and subsequent delocalization of the charge on the oxygen atom to the pyridyl and coumarin moieties.

The highly basic F^- anion acted weakly on compounds **1** and **2** due to its greater hydration than CN^- in aqueous organic solvent (Fig. 8c and d), respectively. However, the HSO_4^- anion caused a greater change in the absorption spectra during titration. The absorption peak at 375–380 nm for both **1** and **2** shifted to a lower wavelength (345 nm) with an increase in intensity, leading to sharp isosbestic points. These changes in absorption spectra were distinct from other anions.

The interactions of **1** and **2** with CN^-, F^- and HSO_4^- were 1 : 1, as confirmed by the Benesi–Hildebrand plots (Fig. S9†).[28] The detection limits[29] for CN^-, F^- and HSO_4^- were in the range of $\sim 10^{-4}$ M for both compounds **1** and **2**, which are significant in anion sensing (Fig. S9†). In the case of CN^-, the detection limits for **1** and **2** were estimated to be 1.23×10^{-4} M and 1.98×10^{-4} M, respectively.

During their interaction, anion-induced deprotonation was confirmed upon the addition of water to the CN^-– and F^--treated solutions of **1** and **2**. The addition of water to the CN^-– and F^--containing solutions of **1** and **2** caused different changes in their UV-vis spectra. Although in the presence of water the original absorption spectra of **1** and **2** were retrieved from F^--containing solutions with a small decrease in intensity, the CN^--containing solutions under similar conditions behaved differently. The CN^--induced red-shifted absorptions in **1** and **2** decreased considerably without showing their original absorption spectra (Fig. S10†). This different behaviour of CN^- was assumed to be due to its participation in deprotonation as well as nucleophilic attack to the imine groups, followed by deprotonation of the phenolic –OH. In the case of HSO_4^-, the original spectra were not restored, which confirmed its different interactional mode from CN^- and F^- (Fig. S11†). HSO_4^- is believed to be involved in H-bonding complexation in the imino-phenol cleft either as HSO_4^- or SO_4^{2-} *via* protonation of the pyridine ring. Fig. 9 represents the different modes of interaction of CN^-, F^- and HSO_4^- with compounds **1** and **2**. In the fluorescence study, no distinguishable change in the emission spectra of **1** and **2** was observed upon the addition of the anions studied (Fig. S12†).

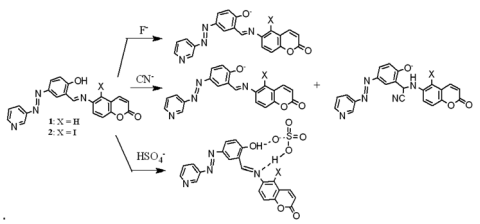

Fig. 9 Different modes of interaction of F^-, CN^- and HSO_4^- (counter cation: tetrabutylammonium ion) with **1** and **2**.

The deprotonation, nucleophilic attack and H-bonding phenomena, as shown in Fig. 9, were finally understood from the ^1H NMR study (Fig. S13, S14, S16, S17 and S18†). The signals for phenolic –OH in **1** and **2** were invisible in the presence of CN^- ions due to their deprotonation. In addition, attack of CN^- to the imine groups in **1** and **2** made the spectra complex to analyse. The appearance of a signal in the range of 5.27–5.86 ppm was ascribed to the CN^- attack to the imine groups. The mass spectra of **1** and **2** in the presence of CN^- revealed the characteristic peaks at m/z = 396.1163 and 522.0378 for (**1** + CN^-–H^+) and for (**2** + CN^-–H^+), respectively. These results confirmed the formation of CN^--adducts through nucleophilic attack of CN^- to the imine bonds (Fig. S19†). The situation was different for the F^- ion, where only deprotonation of the phenolic –OH, followed by hydrogen bonding at a low concentration of F^- occurred, although the signal at ~16–17 ppm for HF_2^- was not found due to significant broadening (Fig. S14†).[30]

Alternatively, the signals of phenolic –OH for **1** and **2** became broad in the presence of the HSO_4^- ion due to the H-bonding instead of deprotonation (Fig. S15 and S18†), respectively. The signal for the –OH proton in **2** showed a downfield chemical shift of 0.05 ppm upon interaction with HSO_4^- (Fig. S18†).

Cu^{2+} and Fe^{3+} ion recognition

The metal ion-responsive behaviour of the DMF–H_2O (2 : 1, v/v) gels of **1** and **2** (prepared at their MGC values) was examined on treatment with 1 equiv. of different metal ions (Fe^{2+} was used as a sulphate salt and other metal ions as perchlorate salts, $c = 0.5$ M). The gel states were intact in the presence of all the tested metal ions. After 10–15 min, the colour of the gels changed from orange yellow to blackish brown only in the presence of Fe^{3+} and Cu^{2+} ions. Other metal ions, under identical conditions, remained silent (Fig. 10a). In this case, the selective color change of the gels is thought to be caused by the charge delocalization from the phenolate oxygen to the pyridyl azo group of **1** and **2** following complexation with Cu^{2+} and Fe^{3+} at the imino-phenol moiety of the gelators. Interestingly, this gel-to-gel color transition started at different lower concentrations of Fe^{3+} and Cu^{2+} ions (Fig. S20†). This study indicates the sensitivity of the gels to Fe^{3+} and Cu^{2+} ions.

However, the addition of TBAF to the Fe^{3+}-induced gels of **1** and **2** resulted in the complete restoration of their colour (blackish brown to orange yellow). Similarly, on adding dodecanethiol to the Cu^{2+}-induced gels of **1** and **2**, the brown gels turned orange yellow. Thus, the use of different chelating species enabled us to discriminate Fe^{3+} from Cu^{2+} ions through the gel-to-gel colour change (Fig. 10b). To establish the selective interaction of Fe^{3+} ions over Fe^{2+} ions, we added Fe^{2+} ions to both gels of **1** and **2** and no distinct colour change was observed. When *m*-CPBA was added to the Fe^{2+}-treated gels of **1** and **2**, a blackish brown colour appeared in the same way as Fe^{3+} ions (Fig. S21 and S22†). However, the addition of *m*-CPBA to the gels

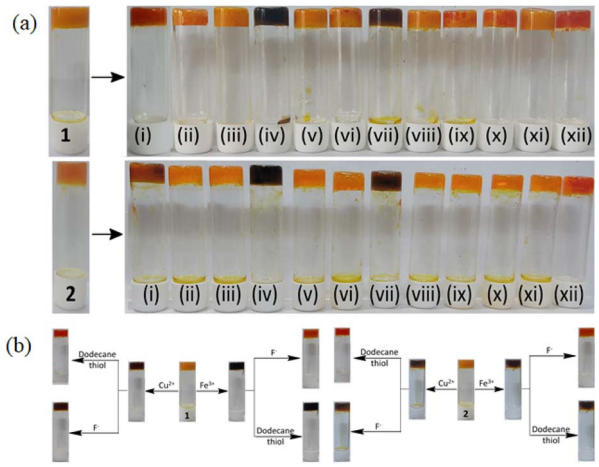

Fig. 10 (a) Photographs of the gel-to-gel color changes in gels **1** (5 mg mL^{-1}) and **2** (6 mg mL^{-1}) in DMF–H_2O (2 : 1, v/v) in the presence of 1 equiv. amount of different metal ions: [(i) Fe^{2+}, (ii) Hg^{2+}, (iii) Zn^{2+}, (iv) Fe^{3+}, (v) Cd^{2+}, (vi) Pb^{2+}, (vii) Cu^{2+}, (viii) Al^{3+}, (ix) Ni^{2+}, (x) Co^{2+}, (xi) Ca^{2+} and (xii) Ag^{+} (in this study, Fe^{2+} was taken as a sulphate salt and other metal ions were taken as perchlorate salts)]; (b) distinction between Cu^{2+} and Fe^{3+} ions using the gels of **1** (left) and **2** (right) in DMF–H_2O (2 : 1, v/v).

of **1** and **2** did not show any colour change. This study was useful for the distinction of Fe^{2+} from Fe^{3+} ions.[6e]

UV-vis and fluorescence studies were performed to investigate the solution phase interactions of **1** and **2** with the above-mentioned metal ions. In this study, the metal ions were added gradually up to 20 equiv. to solutions of **1** and **2** in DMF–H_2O (2 : 1, v/v). Importantly, there were no significant and distinguishable changes in the absorption and emission spectra in DMF–H_2O (2 : 1, v/v) (Fig. S23 and S24†), respectively. In the fluorescence spectra, metal ions quenched the emission, and in the case of **1**, its emission was quenched more by Fe^{3+} ions than the other metal ions. In comparison, this was not observed with compound **2**. The Stern–Volmer plots[31] in Fig. S25† clearly explain this. Thus, compounds **1** and **2** are suitable to recognize Cu^{2+} and Fe^{3+} ions in the gel state rather than in the solution phase. Although there was no selective recognition of metal ions in solution, we performed the Jobs plot[32] analysis for Cu^{2+} and Fe^{3+} ions to understand their interactional properties with the gelators in the gel state. Both metal ions had 2 : 1 (ligand : metal ion) stoichiometric interactions with **1** and **2** (Fig. S26†). The binding constant[33] values for Cu^{2+} (compound **1**: $K_{11} = 4.25 \times 10^3\ M^{-1}$, $K_{21} = 1.89 \times 10^4\ M^{-1}$; compound **2**: $K_{11} = 7.12 \times 10^3\ M^{-1}$, $K_{21} = 1.38 \times 10^3\ M^{-1}$) and Fe^{3+} (compound **1**: $K_{11} = 1.25 \times 10^5\ M^{-1}$, $K_{21} = 1.85 \times 10^5\ M^{-1}$, compound **2**: $K_{11} = 3.55 \times 10^4\ M^{-1}$, $K_{21} = 1.69 \times 10^5\ M^{-1}$) were observed to be considerable (Fig. S27†).

However, to acquire a better understanding of the interactions of the compounds with Cu^{2+} and Fe^{3+}, we attempted to crystallize compounds **1** and **2** in their presence. We were only successful in isolating crystals of **2** with Cu^{2+}. The single-crystal X-ray analysis revealed that it was crystallized in the triclinic $P\bar{1}$ space group (Table S3†). Its asymmetric unit contains one copper atom encircled by two molecules involving phenolic –OH and imine nitrogen as the coordinating centres (Fig. 11a). Two coumarins in its crystal are anti-periplanar, showing a dihedral angle of 62.15° with the azo unit (Fig. 11b). In the crystal packing, hydrogen and halogen bonds play important roles. Molecules are connected to each other through these two weak interactions, forming a supramolecular network (Fig. 11c). Despite the presence of a pyridine ring, the halogen bonding involving the pyridine ring nitrogen is absent in the network. The iodine atom is bonded to coumarin *via* the ester oxygen, showing a distance of 3.07 Å. In addition to this halogen bond, C–H, *para* to the C–I bond of the coumarin unit of one molecule is selectively involved in H-bonding with the phenol oxygen of other molecule to form the assembly.

To understand the intermolecular interactions and the role of halogen bonding, Hirshfeld surface (HS) analysis was carried out on the Cu^{2+} complex of **2**.[34] This was done using one molecular unit. The computed Hirshfeld surfaces (d_{norm}, shape index, curvedness, and fragment patch) (Fig. S28†) and the fingerprint plots (Fig. S29†) reveal the quantitative and qualitative contributions of the non-covalent interactions present in the crystal system. The red, blue, and white colors in d_{norm} indicate whether an interatomic distance is shorter, longer, or equal to a van der Waals separation, respectively. Molecular sculpting can be further illuminated chemically useful the curvature parameters such as shape-index and curvedness. The dark-blue boundaries in the shape index (Fig. S28†) emphasize the high degree of curvature and demonstrate the flatness of the surface with "bumps and hollows", which belong to blue and red, respectively. The curvedness usually indicates large, flat green regions with dark-blue edges surrounding them. The d_{norm} mapped surface is shown in Fig. S28† with the red patches near the oxygen atoms, indicating the presence of O···H/H···O interactions. The O···H contact between the C–H hydrogen of

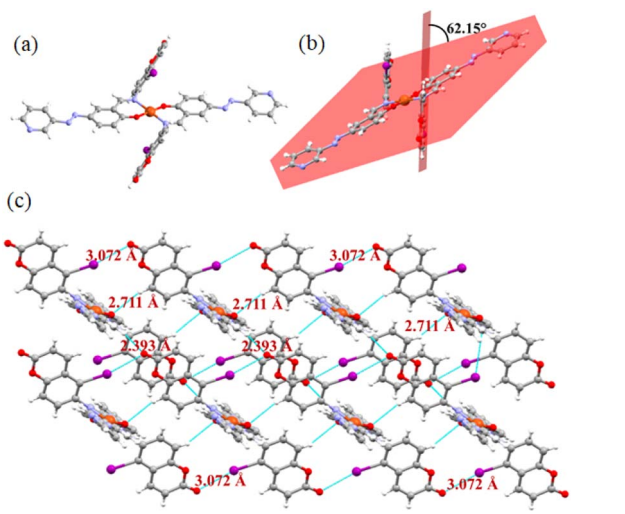

Fig. 11 (a) Pictorial representation of the Cu^{2+}-complex; (b) dihedral angle between coumarin and the other part of the molecule; and (c) supramolecular network of the complex involving halogen and H-bond interactions.

the aldehyde and carbonyl oxygen atoms is supported by the 2D fingerprint plot (Fig. S29d†) as the major interaction (15.2%). Additionally, the O···H/H···O hydrogen bonding interactions show a sharp spike at ($d_i = 1.30$ Å, $d_e = 0.90$ Å) and ($d_i = 0.90$ Å, $d_e = 1.30$ Å). Also, the red patches near the iodine atom indicate the I···O/O···I interactions. The I···O interaction (3%) was also supported by the 2D fingerprint plot in Fig. S29f† with a sharp spike at ($d_i = 1.80$ Å, $d_e = 1.30$ Å) and ($d_i = 1.30$ Å, $d_e = 1.80$ Å). The additional contribution to the HS comes from the C···H (22.4%), N···H (13.4%) and I···H (5.3%) interactions.

CO_2 detection

In another study, we used the anion-ensembles of **1** and **2** to sense CO_2. In this case, both compounds **1** and **2** were initially treated with the anions, and then CO_2 was bubbled in these solutions. The changes were monitored by UV-vis. The absorption band at 405 nm decreased with the appearance of a peak at 375 nm when CO_2 was bubbled in solutions of **1** and **2** [$c = 2.50 \times 10^{-5}$ M] in DMF–H_2O (2 : 1, v/v) containing 5 equiv. and 8 equiv. of CN^- (used as tetrabutylammonium salt; $c = 1.0 \times 10^{-3}$ M), respectively (Fig. S27†). During the interaction, the faint yellow solutions of **1** and **2**, which became slightly deep in the presence of CN^-, turned into again light yellow on CO_2 bubbling. However, when CO_2 was removed from these solutions through the bubbling of N_2, the solutions became deep yellow in colour. This bubbling of CO_2 followed by parching of N_2 gas was continued 5 times, which confirmed the reversibility of the interaction of the CN^- ensembles of **1** and **2** with CO_2 (Fig. 12).

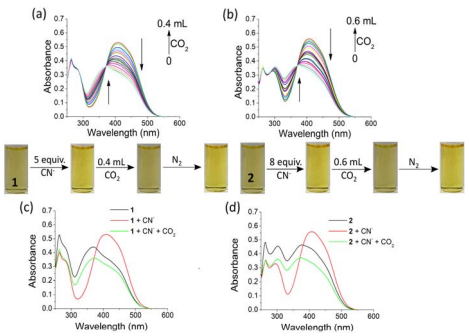

Fig. 12 UV-vis titration spectra of the CN^--ensembles (a) **1** and (b) **2** [$c = 2.50 \times 10^{-5}$ M] in DMF–H_2O (2 : 1, v/v) upon bubbling of CO_2 [ensembles were prepared by adding 6 equiv. and 8 equiv. of CN^- ion [$c = 1 \times 10^{-3}$ M] to solutions of **1** and **2**, respectively]; (c) and (d) highlight the respective color changes and comparative UV-vis spectra of **1** and **2** with the addition of CN^- followed by bubbling of CO_2.

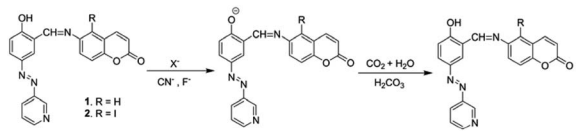

Scheme 2 Mechanism of the interaction of CO_2 with anion-activated compounds **1** and **2**.

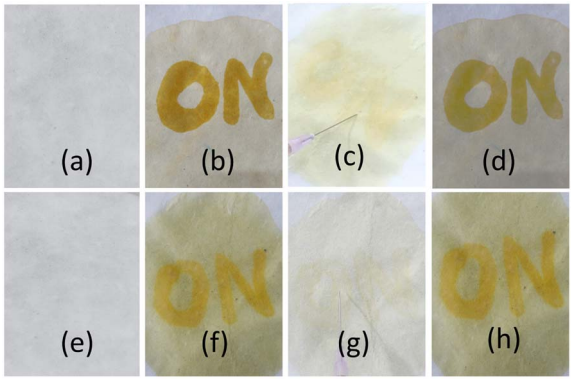

Fig. 13 Pictorial representations for CO_2 sensing *via* the test kit method: invisible writing with CN^- solution on the papers (a and e); contact with DMF solutions of **1** and **2** (b and f); blowing of CO_2 with a syringe (c and g) and parching of N_2 to remove CO_2 (d and h).

The CN^--induced deprotonated forms of **1** and **2** that coexist with CN^--adducts were reprotonated by HCO_3^-, formed from the reaction of CO_2 with trace level of water and showed a color change (Scheme 2). This is in accordance with the previous observations.[23] We successfully developed a paper test-kit for the practical detection of CO_2 (Fig. 13). In this method, a letter was written on a paper using a CN^- solution, prepared in DMF. Then, it was treated with solutions of **1** and **2** in DMF. The invisible letter became visible, whereas it vanished when CO_2 was blown on it. The letter reappeared on keeping the paper strip under N_2 flash. This reversible process was repeated several times, indicating the chemical stability of this paper strip under the stimuli of CN^- ions, CO_2 and N_2.

Conclusions

In summary, we synthesized 6-aminocoumarin-based Schiff bases **1** and **2**, which formed stable thermo-reversible gels in different organic-aqueous mixture solvents. The gels exhibited good elastic properties. The rheological study revealed that the DMF–H_2O (2 : 1, v/v) gel of **2** (iodo-analogue) had a higher resistance value against external forces compared to the gel of **1** (non-iodo analogue). Iodo-analogue **2** showed a cross-linked helical morphology, whereas non-iodo compound **1** showed a long chain fibrous morphology. The gels were stable in a wide pH range (2.6–8). Above pH 8, the gel of **2** started to disintegrate and became a clear solution at pH 13.8, whereas under this condition there was some sticky mass in **1**. This difference in **2** from **1** is due to the halogen bonding role of iodine, which was understood from theoretical study. This subtle effect of iodine in aggregation to afford a mechanically strong gel is unknown in 6-aminocoumarin-based structures. Concerning the iodo-effect on the aggregation, only few examples having iodine-containing triazoles are known in the literature.[35a,b] In the majority of cases, the halogen bonding effect in supramolecular gel formation focused on multi-component systems, where one of them is iodoperfluoroarene.[35c]

To demonstrate their application, gels of **1** and **2**, prepared in DMF–H_2O (2 : 1, v/v), were anion-responsive, showing a gel-to-sol phase change selectively in the presence of CN^-. Compared to the gel state, there was no anion-binding selectivity in solution, although HSO_4^- showed different UV-vis spectral features compared to F^- and CN^-. The considerable changes in the absorption spectra of both compounds in the presence of CN^- are notable for its distinction from F^-.

Besides anion-responsiveness, the gels of **1** and **2** recognized Cu^{2+} and Fe^{3+} ions by showing a gel-to-gel colour change, although no distinguishable feature of metal ion recognition was observed in solution. The crystal structure analysis of the copper complex of **2** revealed the impressive binding of Cu^{2+} and aggregation of the complex involving H-bonding and halogen bonds. For the wide application of **1** and **2**, anion-activated solutions of **1** and **2** were explored for the naked-eye detection of CO_2. In this context, a test-kit for CO_2 sensing was developed. Thus, 6-aminocoumarin-based compounds **1** and **2** serve as excellent gelators, enabling the recognition of CN^-, Cu^{2+} and Fe^{3+} ions in the gel state and CO_2 sensing with good efficiency in solution.

Experimental

Materials and methods

All chemicals and reagents were purchased from Spectrochem, India. The tetrabutylammonium (TBA) salts of the anions were purchased from Sigma-Aldrich. The solvents used in the synthesis were purified, dried and distilled before use. ^1H and ^{13}C NMR spectra were recorded using a Bruker 400 MHz instrument. FTIR measurements of the compounds were carried out using a Perkin-Elmer L120-00A spectrometer (ν_{max} in cm^{-1}). Scanning electron microscopy (SEM) images were obtained on an EVO LS-10 ZEISS instrument. Fluorescence and UV-vis studies were performed using a Horiba Fluoromax 4C spectrofluorimeter and Shimadzu UV-2450 spectrophotometer, respectively. Rheological studies were carried out with a Malvern, KINEXUS Pro+ instrument using a parallel plate (8 mm).

Synthesis

Compounds **3** [36] and **4** [37] were prepared according to the reported procedures. Pyridyl-azo salicylaldehyde **5** was prepared by us, as reported earlier.[38]

Compound 1. Compound **3** (1.0 g, 6.2 mmol) and pyridyl-azo salicylaldehyde **5** (1.69 g, 7.4 mmol) were added to 25 mL of dry MeOH in a 100 mL round-bottom flask. The reaction was stirred at room temperature for 2 h. After completion of the reaction, the volume of the solvent was reduced to some extent. The orange-coloured precipitate was filtered and washed several times with methanol and dried in the open air to get Schiff base **1** (2.0 g, yield of 86%, mp of 230 °C). ^{1}HNMR ($CDCl_3$, 400 MHz): δ 13.48 (s, 1H), 9.10 (d, 1H, $J = 1.6$ Hz), 8.74 (s, 1H), 8.63 (d, 1H, $J = 3.6$ Hz), 8.08–8.01 (m, 3H), 7.69 (d, 1H, $J = 8$ Hz), 7.47 (dd, 1H, $J_1 = 8.4$, $J_2 = 2.4$), 7.40–7.36 (m, 3H), 7.12 (d, 1H, $J = 8.8$ Hz), 6.45 (d, 1H, $J = 9.6$ Hz); ^{13}C NMR ($CDCl_3$, 100 MHz): δ 164.3, 162.7, 160.2, 153.0, 151.4, 147.8, 147.0, 145.7, 144.2, 142.8, 128.4, 128.0, 126.8, 124.6, 123.9, 120.0, 119.5, 118.7, 118.4, 118.1, 117.7; FTIR (KBr, ν cm^{-1}): 3430, 3069, 1721, 1633, 1096, 833; HRMS (TOF MS ES$^+$): calculated $C_{21}H_{15}N_4O_3$ [M + H$^+$] 371.1139, found 371.1133 [M + H$^+$].

Compound 2. Compound **4** (1.0 g, 3.48 mmol) and pyridyl-azo salicylaldehyde **5** (0.950 mg, 4.18 mmol) were added to 25 mL of dry MeOH in a 100 mL round-bottom flask. The reaction was stirred at room temperature for 2 h. After completion of the reaction, the volume of the solvent was reduced. The deep-red-colored precipitate was filtered and washed several times with methanol and dried in open air to get **2** (1.4 g, yield of 81%, mp of 218 °C). ^1H NMR (DMSO, 400 MHz): δ 13.42 (s, 1H), 9.11 (s, 1H), 9.09 (s, 1H), 8.73 (d, 1H, $J = 4.4$ Hz), 8.39 (d, 1H, $J = 2$ Hz), 8.19–8.17 (m, 2H), 8.09 (d, 1H, $J = 8.8$ Hz), 7.80 (d, 1H, $J = 8.8$ Hz), 7.64–7.58 (m, 2H), 7.23 (d, 1H, $J = 8.8$ Hz), 6.62 (d, 1H, $J = 10$ Hz); ^{13}C NMR (d_6-DMSO, 100 MHz): δ 164.1, 160.5, 152.0, 147.9, 147.8, 147.0, 146.3, 146.1, 145.3, 130.3, 127.4, 125.1, 124.8, 123.0, 121.3, 118.9, 118.7, 117.7, 117.6 (two carbons are unresolved); FTIR (KBr, ν cm^{-1}): 3446, 3330, 3200, 2070, 1729, 1613, 1407, 1186, 1111; HRMS (TOF MS ES$^+$): calculated $C_{21}H_{14}N_4O_3$ [M + H$^+$] 497.0105, found 497.0108 [M + H$^+$].

General procedure for gelation test and SEM imaging

An adequate amount of compounds **1** and **2** was dissolved in the desired solvent (1 mL) by warming, and then a co-solvent was added and cooled to room temperature to form a gel. The gel was primarily confirmed by a vial inversion test. The gel-to-sol transition temperature (T_g) for both **1** and **2** was measured by the dropping ball method. The gel samples for SEM imaging were dried under vacuum, and then coated with a thin layer of gold metal.

The anion interaction of the gels was examined either by adding the required amount of anions to the top of the gels or the gels were prepared in the presence of the anions.

Firstly, to confirm the interaction of anions with the gel state, DMF–H_2O (2 : 1, v/v) gels of **1** and **2** were prepared at their minimum gelation concentrations. Then, the gels were treated with 1 equivalent of different anions such as CN^-, F^-, AcO^-, $H_2PO_4^-$, HSO_4^-, NO_3^-, Cl^-, Br^-, and I^- [all were used as tetrabutylammonium (TBA) salt]. Alternatively, compounds **1** (5 mg) and **2** (6 mg) were dissolved in DMF (0.66 mL), followed by the addition of 0.34 mL of water containing 1 equivalent of different anions with respect to gelators **1** ($c = 1.35 \times 10^{-2}$ M) and **2** ($c = 1.20 \times 10^{-2}$ M). In both cases, the gel was not observed in the CN^--containing vial. Either the gel was disintegrated or not formed on contact with CN^-.

General procedures for UV-vis and fluorescence titrations

Stock solutions of compounds **1** and **2** were prepared in DMF–H_2O (2 : 1, v/v) at the concentration of 2.5×10^{-5} M. Stock solutions of tetrabutylammonium salts of anions and perchlorate salts of metal ions were prepared in the same solvents at the concentration of 1×10^{-3} M. In the experiments, 2 mL of the stock solution of compound was added to a cuvette, and to this solution different anions/metal ions were added individually.

Upon the addition of the anions/metal ions, absorption spectra were recorded at room temperature. The same stock solutions were used to perform the fluorescence titration experiments.

Calculation of detection limit[29]

The detection limit was calculated using the UV-vis titration data. The absorbance of the compound was measured 5 times, and the standard deviation of the blank measurement was achieved. To obtain the slope, the absorption intensities were plotted with the concentration of anion. The detection limit was calculated using the equation: detection limit $= 3\sigma/k$, where σ is the standard deviation of the blank measurement and k is the slope.

pK_a determination[27]

The pK_a values were determined according to the following equation: $pK_a = pH + \log[(A_{HB+} - A_x)/(A_x - A_B)]$, where A_{HB+}, A_x and A_B represent the absorbance of the absolute acid and base forms, respectively, at the pH chosen. The pH values were recorded using a pH meter. The pK_a values were derived from non-linear curve fitting of these data (Origin 6.1).

Single-crystal preparation and X-ray diffraction studies

The single crystal of the Cu-complex of **2** was obtained from a $CHCl_3$-petroleum ether (4 : 1, v/v) mixed solvent. To a solution of compound **2** (20 mg, 0.04 mmol) in 10 mL of $CHCl_3$–CH_3OH (95 : 5 v/v), $Cu(ClO_4)_2$ (15 mg, 0.04 mmol) was added. The resulting mixture was stirred for 3 h at room temperature. The precipitate obtained was filtered and dissolved in $CHCl_3$. Then, 2 mL of the resulting solution was added to a narrow-necked glass vial and 500 μL of petroleum ether was added to it. The vial was kept undisturbed. After 10 days, brown crystals were obtained and isolated for data collection.

Crystal data were collected on a Bruker D8 Quest diffractometer configured with a PHOTON 100 detector device, equipped with Mo-Kα ($\lambda = 0.71069$) radiation. The data integration and oblique incidence correction were done using the APEX4 software.[39] Lorentz and polarization effects were considered for data correction, and empirical absorption corrections were applied using SADABS[40] from Bruker. Data collection and data reduction were done using the Bruker Smart Apex and Bruker Saint packages.[39] The structure solution was done by direct methods using the SIR-97 (ref. 41) program and refinement was performed by the full-matrix least-squares methods on F^2 with SHELX[42,43] and Olex 2.[44] The difference Fourier map was used to locate the hydrogen atoms. Hydrogen atoms of the complexes were included in idealized positions and refined as riding models. All figures were drawn using the Mercury software.[45] The crystallographic data including data collection and structure refinement parameters for the Cu-complex of **2** are given in Table S3† [CCDC number 2361386].

Hirshfeld surface (HS) analysis

The various non-covalent interactions within a crystal system are visually represented and quantified through Hirshfeld surface analysis. The Hirshfeld surface (HS), constructed from the electron distribution analysis around a molecule, visualizes the intermolecular interactions in molecular crystals. The two-dimensional (2D) fingerprint plots are obtained from the HS analysis which identify each type of intermolecular interaction within supramolecular and coordination compounds. The Hirshfeld surfaces and their corresponding 2D fingerprint plots were calculated over the constituent ionic and molecular geometries using the CRYSTAL EXPLORER 17.5 software package.[34] The properties such as normalized contact distance, shape index, curvedness, and fragment patch were mapped over the Hirshfeld surface and plotted with the appropriate color scale. The 2D fingerprint plots were presented as d_e *vs.* d_i.

Theoretical study

The geometry optimization of compounds **1** and **2** was performed using the Gaussian 09 package[26] based on DFT (density functional theory). The B3LYP hybrid functional[46] with the 6-31G(d) localized basis function for non-metal (C, N, O, and H) and LANL2DZ basis set with effective core potential was used for iodine. The aggregation processes of **1** and **2** were calculated employing the B3LYP-D3[47] functional. To understand the explicit solvent effects, water molecules were added to the solution and aggregated forms. To confirm the energy minima of the optimized geometries, frequency calculations were performed. With the optimized geometries, time-dependent density functional theory (TD-DFT) was carried out using the 30 lowest singlet excitations.

Data availability

The data supporting this article have been included as part of the ESI.† Crystallographic data for the Cu^{2+}-complex of compound **2** have been deposited at the CCDC under the number 2361386.

Conflicts of interest

There are no conflicts to declare.

Acknowledgements

EP thanks UGC, India for providing fellowship. KG thanks SERB, New Delhi, India for financial support [CRG/2021/005928/OC Dated 20.12.2021] in the laboratory. We also thank DST, New Delhi for providing facilities under FIST program (Level-II, SR/FST/CS-II/2019/96).

References

1 (*a*) Y. Wang, J. Xiong, F. Peng, Q. Li and M.-H. Zeng, *Colloids Surf., A*, 2022, **640**, 128445; (*b*) C. Y. Bao, R. Lu, M. Jin, P. C. Xue, C. H. Tan, Y. Y. Zhao and G. F. Liu, *Carbohydr. Res.*, 2004, **339**, 1311; (*c*) I. A. Duceac and S. Coseri, *Gels*, 2022, **8**, 779; (*d*) S. Ghosh, N. Baildya and K. Ghosh, *RSC Sustainability*, 2023, **1**, 914.

2 (*a*) M. Xue, Y. Lu, Q. Sun, K. Liu, Z. Liu and P. Sun, *Cryst. Growth Des.*, 2015, **15**, 5360; (*b*) J. Zhang and C.-Y. Su, *Coord. Chem. Rev.*, 2013, **257**, 1373.

3 (*a*) H. Qian and I. Aprahamian, *Chem. Commun.*, 2015, **51**, 11158; (*b*) H. Wu, B. B. Ni, C. Wang, F. Zhai and Y. Ma, *Soft Matter*, 2012, **8**, 5486.

4 (*a*) J. Xie, C. Chen, X. Ma and J. Wu, *Inorg. Chem. Commun.*, 2016, **65**, 41; (*b*) A. Panja and K. Ghosh, *New J. Chem.*, 2019, **43**, 5139.

5 (*a*) W. Chen, W. Gong, J. Ye, Y. Lin and G. Ning, *RSC Adv.*, 2012, **2**, 809; (*b*) C. Pati and K. Ghosh, *New J. Chem.*, 2019, **43**, 2718.

6 (*a*) J. Sun, Y. Liu, L. Jin, T. Chen and B. Yin, *Chem. Commun.*, 2016, **52**, 768; (*b*) X. Cao, A. Gao, J.-T. Hou and T. Yi, *Coord. Chem. Rev.*, 2021, **434**, 213792; (*c*) X. Cao, Y. Li, A. Gao, Y. Yu, Q. Zhou, X. Chang and X. Hei, *J. Mater. Chem. C*, 2019, **7**, 10589; (*d*) X. Cao, Y. Li, Y. Yu, S. Fu, A. Gao and X. Chang, *Nanoscale*, 2019, **11**, 10911; (*e*) A. Panja and K. Ghosh, *Mater. Chem. Front.*, 2018, **2**, 2286.

7 K. Hawkins, A. K. Patterson, P. A. Clarke and D. K. Smith, *J. Am. Chem. Soc.*, 2020, **142**, 4379.

8 P. Xue, R. Lu, G. Chen, Y. Zhang, H. Nomoto, M. Takafuji and H. Ihara, *Chem.–Eur. J.*, 2007, **13**, 8231.

9 (*a*) M. O. Piepenbrock, G. O. Lloyd, N. Clarke and J. W. Steed, *Chem. Rev.*, 2010, **110**, 1960; (*b*) N. M. Sangeetha and U. Maitra, *Chem. Soc. Rev.*, 2005, **34**, 821; (*c*) M. D. Segarra-Maset, V. J. Nebot, J. F. Miravet and B. Escuder, *Chem. Soc. Rev.*, 2013, **42**, 7086; (*d*) D. K. Smith, *Chem. Soc. Rev.*, 2009, **38**, 684; (*e*) L. Zhang, L. Qin, X. Wang, H. Cao and M. Liu, *Adv. Mater.*, 2014, **26**, 6959.

10 (*a*) J. Y. C. Lim and P. D. Beer, *Chem*, 2018, **4**, 731; (*b*) T. Bunchuay, A. Docker, A. J. Martinez-Martinez and P. D. Beer, *Angew. Chem., Int. Ed.*, 2019, **58**, 13823; (*c*) A. Docker, X. Shang, D. Yuan, H. Kuhn, Z. Zhang, J. J. Davis, P. D. Beer and M. J. Langton, *Angew. Chem., Int. Ed.*, 2021, **60**, 19442; (*d*) S. C. Patrick, R. Hein, A. Docker, P. D. Beer and J. J. Davis, *Chem.–Eur. J.*, 2021, **27**, 10201.

11 (*a*) Y. J. Wang, X. N. Zhang, Y. Song, Y. Zhao, L. Chen, F. Su, L. Li, Z. L. Wu and Q. Zheng, *Chem. Mater.*, 2019, **31**, 1430; (*b*) S. Chen, K. Zhang, Z. Li, Y. Wu, B. Zhu and J. Zhu, *Supramolecular Materials*, 2023, **2**, 100032; (*c*) L. Lu, W. Zhou, Z. Chen, Y. Hu, Y. Yang, G. Zhang and Z. Yang, *Gels*, 2022, **8**, 244; (*d*) S. Bera, S. Basu, B. Jana and P. Dastidar, *Angew. Chem.*, 2023, **62**, e202216447.

12 (*a*) Y. C. Tse, A. Docker, Z. Zhang and P. D. Beer, *Chem. Commun.*, 2021, **57**, 4950; (*b*) M. Kaasik, S. Kaabel, K. Kriis, I. Jarving and T. Kanger, *Synthesis*, 2019, **51**, 2128; (*c*) A. Docker, C. H. Guthrie, H. Kuhn and P. D. Beer, *Angew. Chem., Int. Ed.*, 2021, **60**, 21973; (*d*) L. E. Bickerton, A. Docker, A. J. Sterling, H. Kuhn, F. Duarte, P. D. Beer and M. J. Langton, *Chem.–Eur. J.*, 2021, **27**, 11738.

13 (*a*) Y.-S. Yang, C. Liang, C. Yang, Y.-P. Zhang, B.-X. Wang and J. Liu, *Spectrochim. Acta, Part A*, 2020, **237**, 118391; (*b*) Y. Wang, X. Hao, L. Liang, L. Gao, X. Ren, Y. Wu and H. Zhao, *RSC Adv.*, 2020, **10**, 6109.

14 (*a*) N. Nuñez-Dallos, C. Cuadrado, J. Hurtado, E. Nagles and O. García-Beltran, *Int. J. Electrochem. Sci.*, 2016, **11**, 9855; (*b*) I. Ketata, L. Mechi, T. Ben Ayed, M. Dusek, V. Petricek and R. Hassen, *Open J. Inorg. Chem.*, 2012, **2**, 33; (*c*) L. Yan, X. Li and J. Li, *ChemistrySelect*, 2018, **3**, 10157; (*d*) Y. Wang, X. Hao, L. Liang, L. Gao, X. Ren, Y. Wu and H. Zhao, *RSC Adv.*, 2020, **10**, 6109; (*e*) H. Q. Li, X. Q. Sun, T. Zheng, Z. X. Xu, Y. X. Song and X. H. Gu, *Sens. Actuators, B*, 2019, **279**, 400; (*f*) Y. Wang, Q. T. Meng, Q. Han, G. J. He, Y. Y. Hu, H. Feng, H. M. Jia, R. Zhang and Z. Q. Zhang, *New J. Chem.*, 2018, **42**, 15839; (*g*) A. Pandey, S. K. Asthana, A. Prakash, J. K. Roy, I. Tiwaria and K. K. Upadhyay, *Dalton Trans.*, 2019, **48**, 2068; (*h*) A. Mondal, S. Nag and P. Banerjee, *Dalton Trans.*, 2021, **50**, 429; (*i*) F. Fu, X. Zhang, S. Zhou, W. Shi, J. Li, J. Yu, Y. Rao, L. Wu and J. Cao, *New J. Chem.*, 2022, **46**, 5034.

15 M. K. Paul, Y. D. Singh, A. Dey, S. K. Saha, S. Anwar and A. P. Chattopadhyay, *Liq. Cryst.*, 2016, **43**, 343.

16 (*a*) R. Koenig, *Science*, 2000, **287**, 1737; (*b*) C. Young, L. Tidwell and C. Anderson, *Minerals*, Metals, and Materials Society: Warrendale, 2001; (*c*) WHO 2003, *Cyanogen Chloride in Drinking-Water*, Background document for preparation of WHO Guidelines for drinking-water quality, World Health Organization, Geneva, WHO/SDE/WSH/03.04/51.

17 S. Panja, A. Panja and K. Ghosh, *Mater. Chem. Front.*, 2021, **5**, 584 and references cited therein.

18 (*a*) J. F. Chen, Q. Lin, H. Yao, Y. M. Zhang and T. B. Wei, *Mater. Chem. Front.*, 2018, **2**, 999; (*b*) M. Suresh, D. Amilan Jose and A. Das, *Org. Lett.*, 2007, **9**, 441; (*c*) P. Mahato, S. Saha, P. Das, H. Agarwalla and A. Das, *RSC Adv.*, 2014, **4**, 36140.

19 K. Młyniec, M. Gaweł, U. Doboszewska, G. Starowicz and G. Nowak, *Vitam. Horm.*, 2017, **103**, 295.

20 (*a*) R. R. Crichton, D. T. Dexter and R. J. Ward, *Coord. Chem. Rev.*, 2008, **252**, 1189; (*b*) D. Touati, *Arch. Biochem. Biophys.*, 2000, **373**, 1; (*c*) E. Beutler, V. Felitti, T. Gelbart and N. Ho, *Drug Metab. Dispos.*, 2001, **29**, 495.

21 P. C. Bull, G. R. Thomas, J. M. Rommens, J. R. Forbes and D. W. Cox, *Nat.Genet.*, 1993, **5**, 327.

22 (*a*) C. Quéré, R. Andrew, P. Friedlingstein, S. Sitch, J. Hauck, J. Pongratz, P. Pickers, J. I. Korsbakken, G. Peters, J. Canadell and A. Arneth, *Earth Syst. Sci. Data*, 2018, **10**, 2141; (*b*) X. Zhou, S. Lee, Z. Xu and J. Yoon, *Chem. Rev.*, 2015, **115**, 7944; (*c*) P. Puligundla, J. Jung and S. Ko, *Food Control*, 2012, **25**, 328.

23 (*a*) M. Lee, S. Jo, D. Lee, Z. Xu and J. Yoon, *Dyes Pigm.*, 2015, **120**, 288; (*b*) X. Zhang, Y. Song, M. Liu, H. Li, H. Sun, M. Sun and H. Yu, *Dyes Pigm.*, 2019, **160**, 799; (*c*) X. Zhang, H. Mu, H. Li, Y. Zhang, M. An, X. Zhang, J. Yoon and H. Yu, *Sens. Actuators, B*, 2018, **255**, 2764; (*d*) X. Zhang, H. Li, H. Mu, Y. Liu, Y. Guan, J. Yoon and H. Yu, *Dyes Pigm.*, 2017, **147**, 40; (*e*) C. Pati, R. Raza and K. Ghosh, *Spectrochim. Acta, Part A*, 2020, **229**, 117910; (*f*) T. Gunnlaugsson, P. E. Kruger, P. Jensen, F. M Pfeffer and G. M. Hussey, *Tetrahedron Lett.*, 2003, **44**, 8909e13; (*g*) Z. Guo, N. R. Song, J. H. Moon, M. Kim, E. J. Jun, J. Choi, J. Y. Lee, C. W. Bielawski, J. L. Sessler and J. Yoon, *J. Am. Chem. Soc.*,

2012, **134**, 17846e9; (*h*) R. Raza, A. Panja, N. Baildya and K. Ghosh, *New J. Chem.*, 2023, **47**, 11515.
24 A. Sarbu, L. Biniek, J.-M. Guenet, P. J. Mésini and M. Brinkmann, *J. Mater. Chem. C*, 2015, **3**, 1235.
25 Y. Huang, J. Xing, Q. Gong, L. C. Chen, G. Liu, C. Yao, Z. Wang, H. L. Zhang, Z. Chen and Q. Zhang, *Nat. Commun.*, 2019, **10**, 1.
26 M. J. Frisch, G. Trucks, H. B. Schlegel, G. Scuseria, M. Robb, J. Cheeseman, G. Scalmani, V. Barone, B. Mennucci and G. Petersson, *Gaussian 09, Revision D. 1*, Gaussian Inc., Wallingford CT, 2009, vol. 27, pp. 34.
27 C. Pati, R. Raza and K. Ghosh, *Spectrochim. Acta, Part A*, 2020, **229**, 117910.
28 P. T. Chou, G. R. Wu, C. Y. Wei, C. C. Cheng, C. P. Chang and F. T. Hung, *J. Phys. Chem. B*, 2000, **104**, 7818.
29 B. Zhu, X. Zhang, Y. Li, P. Wang, H. Zhang and X. Zhuang, *Chem. Commun.*, 2010, **46**, 5710.
30 X. Chen, Y.-C. Liu, J. Bai, H. Fang, F.-Y. Wu and Q. Xiao, *Dyes Pigm.*, 2021, **190**, 109347.
31 J. R. Lakowicz, *Principles of Fluorescence Spectroscopy*, Springer, New York, 3rd edn, 2006.
32 P. Job, *Ann. Chim.*, 1928, **9**, 113.
33 Binding constant was determined using BindFit v5.0, available from **https://app.supramolecular.org/bindfit/**. 2023.
34 (*a*) M. A. Spackman and D. Jayatilaka, *CrystEngComm*, 2009, **11**, 19; (*b*) M. A. Spackman and J. J. McKinnon, *CrystEngComm*, 2002, **4**, 378.
35 (*a*) Y. Huang, Y. Zhang, Y. Yuan and W. Cao, *Tetrahedron*, 2015, **71**, 2124; (*b*) Y. Huang, S. Liu, Z. Xie, Z. Sun, W. Chai and W. Jiang, *Front. Chem. Sci. Eng.*, 2018, **12**, 252; (*c*) J. Zheng, A. Suwardi, C. J. E. Wong, X. J. Loh and Z. Li, *Nanoscale Adv.*, 2021, **3**, 6342.
36 S. Roy, T. K. Mondal, P. Mitra, E. L. Torres and C. R. Sinha, *Polyhedron*, 2011, **30**, 913.
37 N. C. Ganguly, S. K. Barik and S. Dutta, *Synthesis*, 2010, **9**, 1467.
38 S. Ghosh, S. Ghosh, N. Baildya and K. Ghosh, *New J. Chem.*, 2022, **46**, 8817.
39 Bruker, *APEX4, SAINT and SADABS*, BRUKER AXS, Inc., Madison, Wisconsin, USA, 2021.
40 G. M. Sheldrick, *Sadabs., Program for Multi-Scan Absorption Correction of Area Detector Data*, University of Gottingen, Germany, 2002.
41 A. Altomare, M. C. Burla, M. Camalli, G. L. Cascarano, C. Giacovazzo, A. Guagliardi, A. G. G. Moliterni, G. Polidori and R. Spagna, *J. Appl. Crystallogr.*, 1999, **32**, 115.
42 G. M. Sheldrick, Crystal Structure Refinement with SHELXL, *Acta Crystallogr., Sect. C: Struct. Chem.*, 2015, **C71**, 3.
43 International Tables for Crystallography, Vol C, Tables 6.1.1.4, 4.2.6.8, and 4.2.4.2, Kluwer, Boston, 1995.
44 O. V. Dolomanov, L. J. Bourhis, R. J. Gildea, J. A. K. Howard and H. Puschmann, *J. Appl. Crystallogr.*, 2009, **42**, 339.
45 C. F. Macrae, I. Sovago, S. J. Cottrell, P. T. A. Galek, P. McCabe, E. Pidcock, M. Platings, G. P. Shields, J. S. Stevens, M. Towler and P. A. Wood, *J. Appl. Crystallogr.*, 2020, **53**, 226.
46 X. Qian, Y.-Z. Zhu, J. Song, X.-P. Gao and J.-Y. Zheng, *Org. Lett.*, 2013, **15**, 6034.
47 P. E. Hartnett, C. M. Mauck, M. A. Harris, R. M. Young, Y. L. Wu, T. J. Marks and M. R. Wasielewski, *J. Am. Chem. Soc.*, 2017, **139**, 749.